AIAA JOURNAL
Vol. 55, No. 9, September 2017

Comprehensive Study of Cryogenic Fluid Dynamics of Swirl Injectors at Supercritical Conditions

Xingjian Wang*
Georgia Institute of Technology, Atlanta, Georgia 30332
Hongfa Huo†
General Electric Company, Niskayuna, NY 12309
and
Yanxing Wang‡ and Vigor Yang§
Georgia Institute of Technology, Atlanta, Georgia 30332

DOI: 10.2514/1.J055868

A comprehensive study is conducted to enhance the understanding of swirl injector flow dynamics at supercritical conditions. The formulation is based on full-conservation laws and accommodates real-fluid thermodynamics and transport theories over the entire range of fluid states of concern. Liquid oxygen at 120 K is injected into a supercritical oxygen environment at 300–600 K. Detailed three-dimensional flow structures are visualized for the first time in the pressure range of 100–200 atm. A smooth fluid transition from the compressed-liquid to light-gas state occurs, which is in contrast to a distinct interface of phase change at subcritical pressure. Dynamic behaviors of the oscillatory flowfield are explored using the spectral analysis and proper orthogonal decomposition technique. Various underlying mechanisms dictating flow evolution, including shear-layer, helical, centrifugal, and acoustic instabilities, are studied in depth. The hydrodynamic wave motions in the liquid-oxygen film are found to propagate in two different modes: one along the axial direction at the local wave speed; the other in the azimuthal direction and convected downstream at the mean flow velocity. Results show good agreement with the analytical prediction of the overall response transfer function of the swirl injector. The dominant mode of the azimuthal wave is triggered by the natural acoustic oscillation within the injector. Compared with the two-dimensional axisymmetric results, the calculated liquid-oxygen film is thicker and the spreading angle smaller due to the momentum loss and vortical dynamics in the azimuthal direction.

I. Introduction

SWIRL injectors are widely used in many propulsion and power-generation systems, including airbreathing engines [1,2] and liquid rockets [3]. The swirling motion induces outward spreading of the liquid film and produces a center toroidal recirculation zone downstream of the injector, thereby significantly improving mixing and combustion efficiency. Extensive experimental [4–8] studies have been conducted to examine the flow characteristics of swirl injectors, including spreading angle, liquid film thickness, and discharge coefficient, under various geometric and operating conditions.

Kim et al. [9] studied the flow dynamics of liquid swirl injectors, with water as the working fluid. The spreading angle and breakup length of the liquid film issued from the injection exit were measured using direct photography, in the Weber number range of 170–1554 and pressure range of 1–40 bar. As the pressure increased, the spreading angle remained nearly constant until the breakup of the liquid sheet, and then it decreased slightly. The breakup length decreased with the increasing Weber number and pressure due to enhanced aerodynamic force. In addition, the spreading angle increased with increasing Weber numbers.

Kenny et al. [10] examined the effect of ambient pressure on water swirl injection using shadowgraphs. The measured film thickness and discharge coefficient increased with increasing pressure from 1 to 48 bar for a given mass flow rate. Chen and Yang [11] confirmed Kenny et al.'s results [10] by performing a combined theoretical and numerical analysis. They found that variations of the film thickness and spray angle with pressure were closely related to the modification of the velocity profile in the liquid film near the gas–liquid interface due to the alteration of shear stresses with pressure. A semiempirical model was developed to correlate the distributions of velocity and pressure near the gas–liquid interface, and good agreement with experimental observations was achieved.

Cho et al. [12] conducted experimental studies on the surface instability of a swirl injector with cryogenic fluid (liquid nitrogen) at both subcritical and supercritical conditions. Flow images were obtained using high-speed photography. The amplitude of the surface wave of liquid nitrogen was found to be much higher than that in water under the same operating conditions. The flow characteristics changed dramatically when the ambient pressure increased from a subcritical to a supercritical condition. The surface wave immediately downstream of the injector under subcritical conditions disappeared at supercritical pressures. Cho et al. [13] further investigated the dynamic behaviors downstream of the swirl injector at supercritical pressures using the proper orthogonal decomposition (POD) technique. Two different types of instabilities were found: a symmetric ring-shaped mode generated from the Kelvin–Helmholtz instability, and an antisymmetric-shaped mode created by the helical instability.

In spite of the effort made so far, the currently available data are not sufficient to fully illuminate the intrinsic mechanisms of the injector flow dynamics. Analytical and numerical tools are thus required to explore the details of the flow physics, especially under conditions in which experimentally measurements become challenging. Bazarov and Yang [14] studied the linear dynamics of a swirl injector. The flow oscillations in the liquid layer were characterized by a differential equation analogous to that of shallow-water wave propagation. The velocity fluctuations in the tangential entries were found to induce two different types of disturbance propagating

Presented as Paper 2015-1827 at the 53rd AIAA Aerospace Sciences Meeting, Kissimmee, FL, 5–9 January 2015; received 22 November 2016; revision received 9 February 2017; accepted for publication 28 February 2017; published online Open Access 31 May 2017.

*Postdoctoral Fellow, School of Aerospace Engineering. Member AIAA.
†Lead Engineer, Computational Combustion Lab. Senior Member AIAA.
‡Research Engineer, School of Aerospace Engineering. Member AIAA.
§William R. T. Oakes Professor and Chair, School of Aerospace Engineering; vigor.yang@aerospace.gatech.edu. Fellow AIAA (Corresponding Author).

downstream in the vortex chamber: one traveling in the axial direction at the surface wave speed, and the other traveling in the azimuthal direction and convecting in the axial direction at the local flow speed. A similar phenomenon was observed in gaseous swirl injection [15]. Ismailov and Heister [16,17] performed both linear and nonlinear analyses to investigate wave reflection and resonance behaviors in a swirl injector using an abrupt convergence resonance model and a conical convergence resonance model. The primary resonance of the liquid surface wave in the vortex chamber corresponded to a quarter-wave oscillation. The influence of various parameters, including vortex chamber dimensions, convergence angle, nozzle length, injector flow rate, and pulsation magnitude, were carefully evaluated on resonant response characteristics.

The aforementioned analytical studies [14,16,17] were performed for inviscid, incompressible flows, and the effects of real fluids were not considered. Many realistic devices for propulsion applications, however, operate at pressures much higher than the critical points of the injected fluids. This produces a unique set of problems arising from the introduction of thermodynamic nonidealities and transport anomalies [18]. Zong and Yang [19] systematically studied the dynamics of liquid oxygen (LOX) in a swirl injector at supercritical conditions. An axisymmetric configuration was considered. The flow development was characterized by three different (i.e., developing, stationary, and accelerating) regimes. Hydrodynamic instabilities in the LOX film and acoustic oscillations in the gaseous core were analyzed in detail. Huo et al. [20] further studied the dynamic response of the flowfield to external forcing at the inlet. Although much information has been obtained from these studies, the underlying assumption of flow axisymmetry failed to capture azimuthal variations in flow properties and the vortex-stretching mechanism, which was responsible for the energy transfer from large- to small-scale structures in the flowfield.

Wang et al. [21] presented a numerical analysis of a simplex swirl injector and defined complex three-dimensional flow structures under supercritical conditions typical of contemporary rocket engines using cryogenic propellants. The present work extends Wang et al.'s analysis [21] and attempts to provide a more comprehensive investigation of the flow dynamics of a swirl injector in a three-dimensional space. As a specific example, LOX is considered as the simulant. A unified theoretical and numerical framework based on a large-eddy-simulation technique is developed and implemented. Detailed three-dimensional flow structures within and downstream of the injector are characterized for the first time. The dynamic behaviors of LOX are explored using spectral analysis and proper orthogonal decomposition. Various underlying mechanisms dictating the flow evolution are carefully examined and compared to the classical theories.

II. Theoretical and Numerical Framework

The theoretical framework of the present study, which is capable of dealing with supercritical fluid dynamics over the entire range of fluid thermodynamic states of concern, was described by Oefelein and Yang [22]. Large eddy simulation was employed to achieve turbulence closure, with the Favre-filtered governing equations obtained by filtering small-scale motion. The influence of unresolved small-scale motions was modeled using the compressible-flow version of the static Smagorinsky model [23]. Thermodynamic properties, including density, enthalpy, and specific heats, were derived according to fundamental thermodynamics theories. A modified Soave–Redlich–Kwong equation of state was used to close the gradient terms in the thermodynamic formulation. Transport properties, including thermal conductivity and dynamic viscosity, were estimated by an extended corresponding-state principle [18]. The thermodynamic and transport properties were validated and implemented in previous studies [18,24–26].

The numerical framework contains a self-consistent and robust algorithm implementing a preconditioning scheme and a unified treatment of general fluid thermodynamics [27,28]. It employs a density-based finite volume methodology along with a dual-time-step integration technique [29]. Temporal discretization is achieved using a second-order backward difference, and the inner-loop pseudotime term is integrated with a four-step Runge–Kutta scheme. Spatial discretization is obtained by a fourth-order central difference scheme in generalized coordinates. Fourth-order matrix dissipation as developed by Swanson and Turkel [30] is taken to ensure numerical stability and minimum contamination of the solution. Finally, a multiblock domain decomposition technique associated with the message-passing interface for parallel computation is applied to optimize the computational speed.

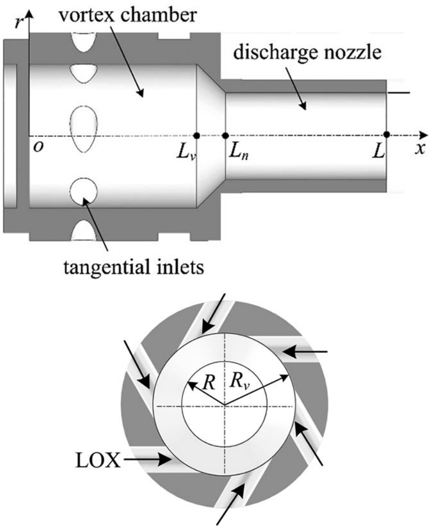

Fig. 1 Simplex LOX swirl injector.

III. Injector Configuration and Boundary Conditions

Figure 1 shows schematically the simplex swirl injector treated in the present study; it mimics the inner swirler of the injector of the RD-0110 LOX/kerosene rocket engine [31]. The injector is a closed-swirl type, consisting of tangential inlets, a vortex chamber, and a discharge nozzle. The contraction angle between the vortex chamber and the nozzle is 45 deg. The baseline geometry and operating conditions are listed in Table 1, where R_v and R represent the radii of the vortex chamber and the discharge nozzle, respectively. L, L_v, and L_n represent the injector length, the vortex chamber length, and the distance between head and nozzle entrance, respectively. T_{in}, T_0, p_0, and $\dot{m}$ denote the inlet temperature, ambient temperature, ambient pressure, and total mass flow rate, respectively. For reference, the critical temperature and pressure of oxygen are 154.6 K and 50.5 bar. LOX at a subcritical temperature (120 K) is delivered through six tangential inlets into the vortex chamber, which is initially filled with gaseous oxygen (300 K).

The computational domain includes the injector interior (8.4R in the axial direction) and a downstream region (25R with 7.4R in the axial and radial directions, respectively). No-slip and adiabatic boundary conditions are applied at the injector surface. The swirl number is about 2.0. At the inlets, the azimuthal and radial velocities are determined from the given mass flow rate and swirl strength. The pressure is obtained from the radial momentum equation. Broadband

Table 1 Baseline geometry and operating conditions

Parameter	Value
R_v, mm	4.5
R, mm	2.7
L, mm	22.7
L_v, mm	10.4
L_n, mm	12.2
T_{in}, K	120
T_0, K	300
p_0, atm	100
$\dot{m}$, kg/s	0.15

noise with a Gaussian distribution is superimposed onto the inlet velocity components to provide the incoming flow structure. The disturbances are produced by a Gaussian random number generator with an intensity of 5% of the mean quantities, which is sufficient to trigger the instability inherent in the flowfield. At the downstream boundary, nonreflecting boundary conditions based on the characteristic equations [32] are applied to avoid undesirable wave reflection by extrapolation of primitive variables from the interior region. A reference pressure is applied to preserve the average pressure in the computational domain.

IV. Grid-Independence Study

The baseline mesh system has 5 million cells, of which 1.7 million cells are located within the injector. The meshes are clustered near the wall, in the mixing layer, and immediately downstream of the injector to resolve steep gradients in these regions. The smallest grid size in the radial direction is 5 μm, as compared to the Taylor scale of 8.4 μm at the injector exit. The computational domain is divided into 636 blocks, with each computed on a single processor. The physical time step is 10^{-6} s and the Courant–Friedrichs–Lewy number is 0.4.

To ensure an appropriate level of accuracy of the predicted flow physics, a grid-independence study was performed. Because considerable computing resources are required for a finer three-dimensional grid system, an axisymmetric study was conducted with identical grid resolution in the radial and axial directions. Periodic boundary conditions were specified in the azimuthal direction. A finer mesh, which doubled the number of cells in both axial and radial directions, was studied as the comparable case. It was noted that the axisymmetric simplification could not capture the azimuthal flow variations and vortex-stretching mechanism, but important injector characteristics and unsteady flow features, including hydrodynamic and acoustic instabilities, were predicted [33,34].

Figure 2 shows the radial distributions of the mean density ρ, temperature T, and velocity components (u_x and u_θ) for the two grid systems at the injector exit. The maximum deviation of all flow properties is less than 5%. The relative errors of the spreading angle and liquid film thickness are below 3%, and the frequency spectrum of the pressure field indicates identical dynamic behaviors. Therefore, the baseline grid system is believed to be sufficient to capture the main characteristics of the LOX injection and mixing process.

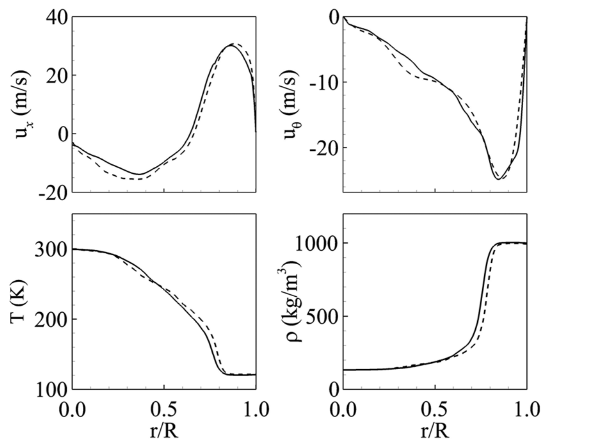

Fig. 2 Radial distributions of time-averaged flow properties at the axial location $x/R = 8.3$ for two grid systems: baseline (solid line), and finer mesh (dashed line).

V. Results and Discussion

A. Supercritical Fluid Regions

Figure 3 shows the instantaneous distribution of oxygen density in both the longitudinal and transverse views. The strong swirling motion and its associated centrifugal force produce a large pressure gradient in the radial direction, causing the LOX film to flow along the injector wall. A low-density gaseous core forms in the center region due to the conservation of mass and angular momentum. The density varies smoothly in the radial direction from a liquid state near the wall to a gaseous state in the core region.

Identification of the transition between the liquid and gaslike fluid states presents some interesting problems. Figure 4 shows the density-temperature (ρ-T) diagram over the pressure range of 20–200 atm. At subcritical pressures ($p < 49.8$ atm), a distinctive liquid/gas transition occurs at the fluid boiling point. The corresponding density gradient shown in Fig. 4b is infinite. At supercritical pressures, the abrupt transition disappears. The density varies continuously with temperature along an isobaric line. To facilitate the discussion, a fluid-state transition is therefore defined to take place in the region where the density gradient is not less than 90% of its maximum magnitude.

Figure 4 shows the transition region (green lines) connecting the liquid state (blue lines) with the gaseous (red lines) state. The transition region becomes wider with increasing pressure, but it degenerates to a sharp interface when the pressure decreases to a subcritical value. For $p = 100$ atm, the upper and lower bounds of density for the transition region are 645 and 450 $\mathrm{kg/m^3}$, respectively. Figure 5 shows the temporal evolution of the density fields on three different transverse planes along the axial axis from the vortex chamber to the discharge nozzle. The area enclosed by the two solid black curves represents the transition region. It is relatively small in the vortex chamber ($x/R = 3.7$) and becomes wider as the LOX film convects downstream. In the downstream region, the shape of the transition region becomes more corrugated due to the shear-layer instability.

B. Instantaneous Flowfield

Figure 6a shows a snapshot of the density field coupled with two density isosurfaces ($\rho = 532$ and 250 $\mathrm{kg/m^3}$). The thickness of the LOX film in the vortex chamber is much larger than that in the discharge nozzle due to the flow acceleration through the converging section and the conservation of mass. The density isosurfaces are corrugated by hydrodynamic instabilities and exhibit complicated wavy structures. Figure 6b shows the isosurface of the azimuthal velocity at 4 m/s on the gaseous side (see Fig. 2). The central gaseous core is highly wrinkled. Helical instability is observed near the injector exit and disappears further downstream due to viscous damping and turbulent dispersion.

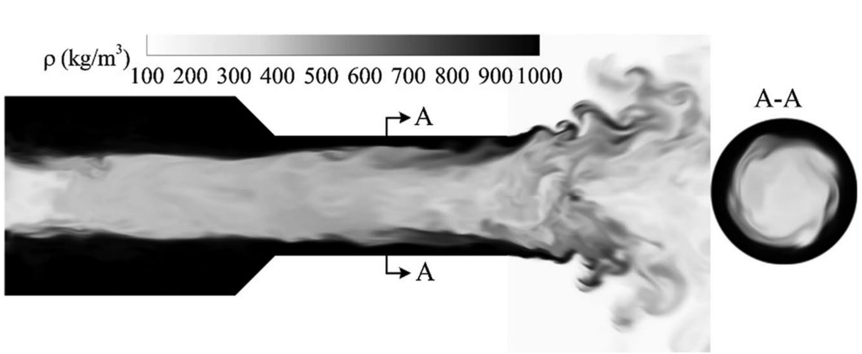

Fig. 3 Snapshot of the density field in longitudinal and transverse views: $p = 100$ atm.

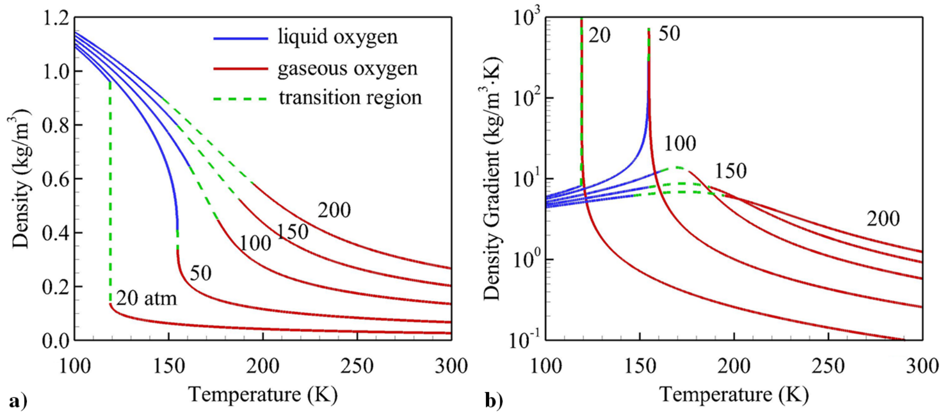

Fig. 4 Representations of the a) density and b) density gradient of oxygen as a function of temperature at various pressures.

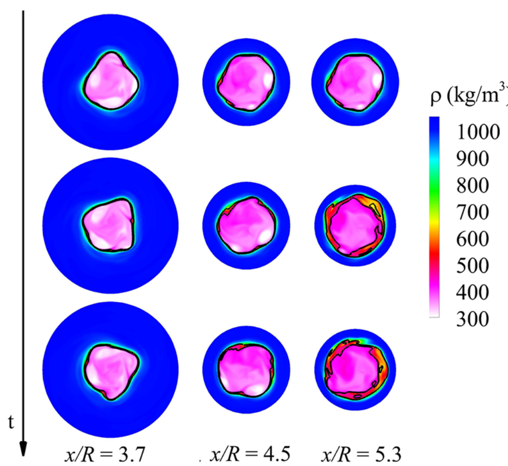

Fig. 5 Temporal evolution of density distributions at different axial locations: $\Delta t = 0.06$ ms, and $p = 100$ atm.

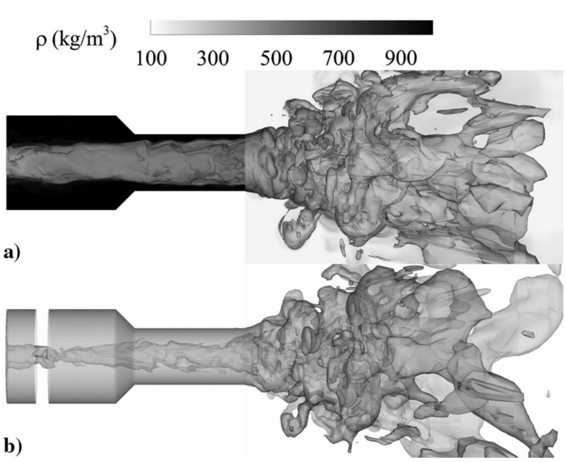

Fig. 6 Snapshots of the a) density field with two isosurfaces ($\rho = 532$ and 250 kg/m^3) and b) instantaneous isosurface of azimuthal velocity at $u_\theta = 4$ m/s ($p = 100$ atm).

Figure 7 shows a snapshot of the vorticity magnitude in different cross sections. The flow evolution exhibits several distinct features, which are similar to those described by Chen and Yang [11] and Zong and Yang [19]. The flowfield in the injector can be divided into four different regimes radially: the wall, free vortex, transition, and forced vortex regions. In the wall region, strong vorticity is produced in the boundary layer. A free vortex is observed next to the wall, where the angular momentum $u_\theta r$ is constant. The tangential velocity u_θ is inversely proportional to the radial distance r, as shown in Fig. 2. In the forced vortex region close to the centerline, on the other hand, the angular velocity remains nearly constant and the tangential velocity is proportional to the radial distance. The transition region connecting the free vortex and forced vortex regions induces the tangential velocity to change smoothly, and a significant vorticity layer is produced in this region. The vorticity layer then exits from the injector, passing off the rim. It subsequently rolls, tilts, stretches, and breaks up into small eddies. These eddies interact and merge with the surrounding flow and finally dissipate further downstream. According to the radial momentum balance,

$$\frac{\partial p}{\partial r} \sim f_c \sim \frac{\rho u_\theta^2}{r} \tag{1}$$

where f_c represents the centrifugal force. The decrease of the azimuthal velocity causes the pressure to recover in the downstream region. The resultant positive pressure gradient decreases the axial velocity in a phenomenon commonly known as vortex breakdown. This creates a center recirculating flow and leads to the rapid dispersion of vorticity in the injector near field.

Figure 8 shows the temporal evolution of streamlines, spatially averaged in the azimuthal direction, during a typical flow evolution period. The time increment between the snapshots Δt is 0.06 ms, and the data collection begins after the flow reaches its stationary state. At $t = \Delta t$, three large bubbles exist downstream of the injector. Small bubbles separate from their parents in the vortex core ($t = 3\Delta t$), travel downstream, and eventually coalesce with large vortex bubbles in the downstream region.

Vorticity dynamics plays an essential role in the determination of flow motion. The vorticity budget is therefore examined to identify the major mechanisms responsible for vorticity production and destruction under supercritical conditions. The transport equation for vorticity magnitude takes the form

$$\frac{\mathrm{D}\boldsymbol{\Omega}\cdot\boldsymbol{\Omega}}{\mathrm{D}t} = 2\boldsymbol{\Omega}\cdot(\boldsymbol{\Omega}\cdot\nabla)U - 2\boldsymbol{\Omega}\cdot\boldsymbol{\Omega}(\nabla\cdot U) - 2\boldsymbol{\Omega}\cdot\nabla\left(\frac{1}{\rho}\right)\times\nabla(p) + 2\boldsymbol{\Omega}\cdot\nabla\times\left(\frac{\nabla\cdot\boldsymbol{\tau}}{\rho}\right) \tag{2}$$

where $\boldsymbol{\Omega}$ is the vorticity, and $\boldsymbol{\tau}$ is the viscous stress tensor. The four terms on the right-hand side represent the effects of vortex stretching/tilting, volume dilatation, baroclinic torque, and viscous dissipation, respectively. For a cryogenic fluid under supercritical conditions, steep property variations occur when the injected fluid is heated by the ambient gas. The ensuing volume dilatation and baroclinic torque are significant in determining vorticity transport. Figure 9 shows the radial distributions of the azimuthally averaged vorticity budget normalized by the bulk velocity and momentum thickness at three different axial locations. Here, the bulk velocity and momentum thickness are taken at the injector exit. Vortex stretching and tilting dominate the shear-layer vorticity production in the vortex chamber ($x/R = 1$) and discharge nozzle ($x/R = 5$). In the injector near field ($x/R = 9$), however, both volume dilatation and baroclinic torque

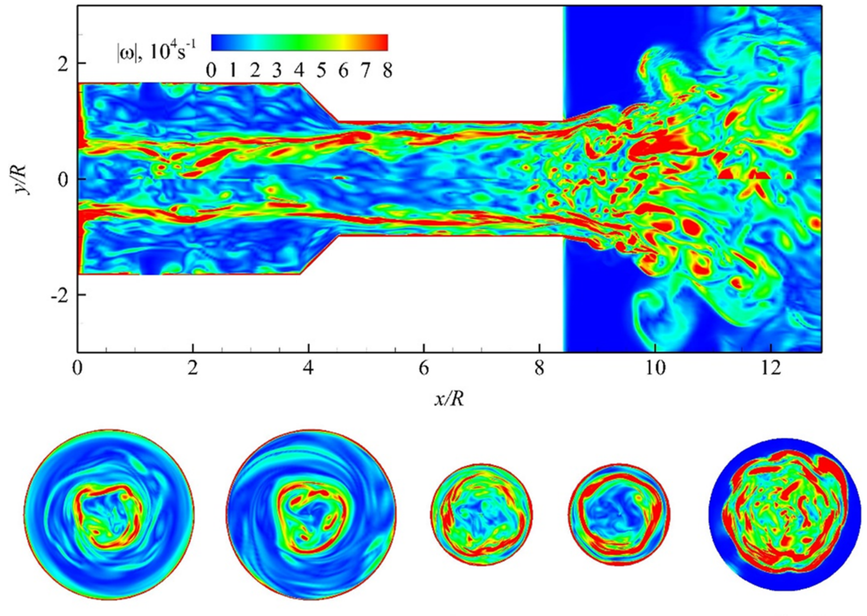

Fig. 7 Snapshots of vorticity magnitude on different cross sections: $p = 100$ atm.

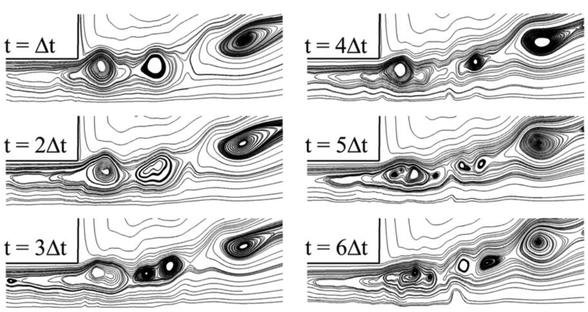

Fig. 8 Temporal evolution of streamlines spatially averaged in the azimuthal direction: $\Delta t = 0.06$ ms, and $p = 100$ atm.

become significant in the outer shear layer, where the LOX film mixes with ambient gaseous oxygen.

C. Flow Instability and Wave Characteristics

As shown in Fig. 6, the LOX film is intrinsically unstable and features three-dimensional hydrodynamic instability waves. Figure 10 shows the isosurface of the azimuthal velocity at 22 m/s within the LOX stream, with the physical domain in the azimuthal direction unwrapped. Generally, a flow variable can be expressed by a Fourier series in the cylindrical coordinate system (x, r, θ):

$$G(x, r, \theta, t) = \sum_{m=-\infty}^{\infty} g_m(x, r, t) e^{im\theta} \tag{3}$$

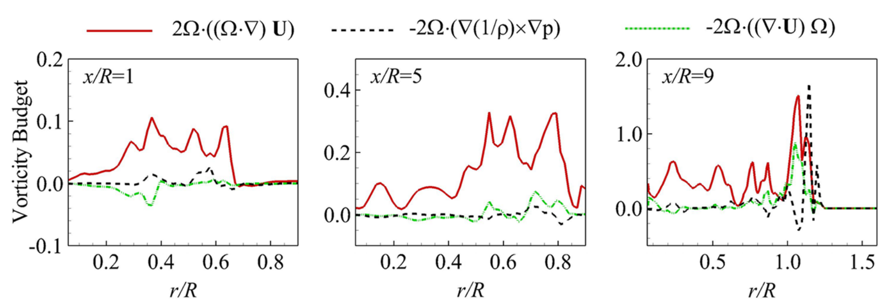

Fig. 9 Radial distributions of vorticity magnitude spatially averaged in the azimuthal direction at three different axial locations: $p = 100$ atm.

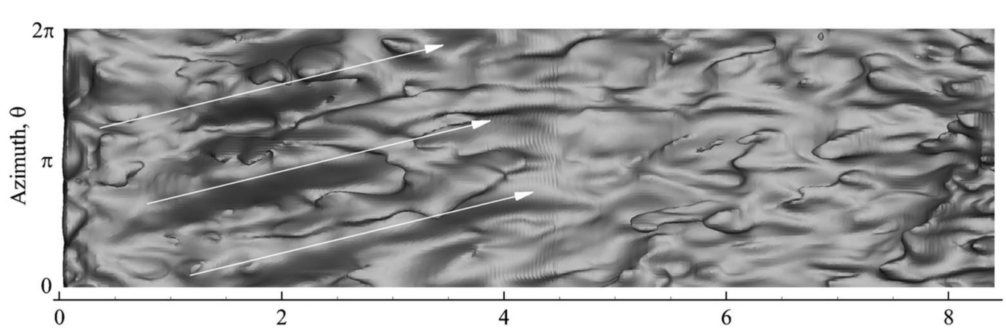

Fig. 10 Isosurface of azimuthal velocity at $u_\theta = 22$ m/s in the azimuthal plane ($\theta = 0$–2π): $p = 100$ atm.

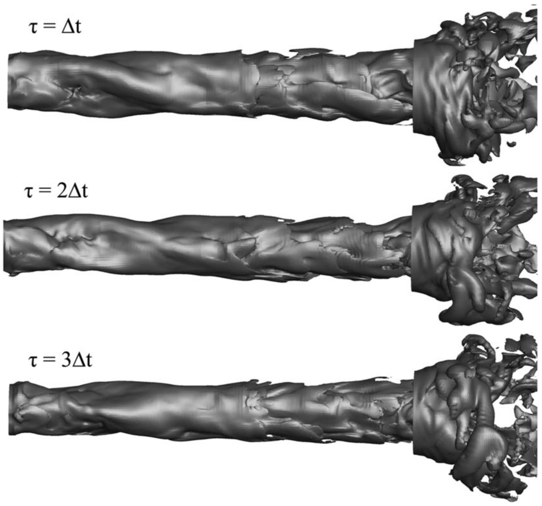

Fig. 11 Temporary evolution of density isosurface at $\rho = 532\ \mathrm{kg/m^3}$, $\Delta t = 0.06$ ms, and $p = 100$ atm.

where g_m is the Fourier coefficient, and m is the azimuthal wave number. Note that $m = 0$ represents the axisymmetric mode, and the others ($m \neq 0$) represent the helical modes. In the vortex chamber ($x \leq 10.4$ mm), three helical waves coupled with small-scale structures are observed, as evidenced by the three major structures around $x = 5$ mm (marked by white arrows), indicating that the helical mode $m = -3$ dominates the flowfield. It will be shown that this specific helical mode is triggered by the acoustic wave with the same frequency. In the discharge nozzle ($x \geq 10.5$ mm), the higher axial velocity accelerates the spiral structure, leading to the bendover of the wave shape. The helical waves are distorted by the strong shear layer between the LOX film and gaseous core.

To further explore the underlying flow physics, hydrodynamic waves in the axial and azimuthal directions are analyzed separately. Figure 11 shows the temporal evolution of the density isosurface at $\rho = 532\ \mathrm{kg/m^3}$, located in the interfacial layer between the liquid and gaseous oxygen (see Fig. 2). A spiral shape forms in the vortex chamber, whereas a cone-shaped surface is produced with ligaments in the discharge nozzle. (See Figs. 3 and 6 for the injector profile.) This shape change is related to the Kelvin–Helmholtz (KH) shear-layer instability in the flow transition region. The flow motion is swirl dominated with low axial momentum in the vortex chamber, and hence the axial KH instability is relatively weak and induces a smooth isosurface. The LOX film accelerates rapidly through the converging nozzle, rendering a strong KH instability in the discharge nozzle. The baroclinicity resulting from the misalignment of the density and pressure gradients also contributes to the flow instability. The respective significance of these effects can be seen in the vorticity budget, as shown in Fig. 9.

The disturbance wave speed can be determined empirically. For an inviscid, incompressible flow, neglecting the radial velocity and assuming an infinitesimal film thickness compared to the wavelength, the form of the wave speed bears a close resemblance to that for shallow-water wave propagation [14], and it is expressed explicitly as

$$a_x = \sqrt{\left(\frac{u_{\mathrm{in}}^2 R_{\mathrm{in}}^2}{r_m^3}\right)\left(\frac{r^2 - r_m^2}{2r_m}\right)} \tag{4}$$

Here, u_{in} (20 m/s), R_{in} (3.5 mm), and r_m represent the inlet velocity, swirling arm, and radius of the liquid film surface, respectively. Also, r denotes the radius of the injector (R_v in the vortex chamber and R in the discharge nozzle). The computed wave speed in the vortex chamber ($r_m = 1.61$ mm) and discharge nozzle ($r_m = 1.94$ mm), from Eq. (4), are 80 and 25 m/s, respectively. These wave speeds do not rely on the disturbance frequency, although Ismailov and Heister [35] found that implementing the classical Kelvin's dispersion relation between the angular frequency and wave number caused the wave speed to decrease slightly with increasing frequency. As shown in the next section, the dominant frequency of the disturbances is 0.9 kHz. The actual wave speeds in both the vortex chamber and the nozzle are smaller than those predicted by Eq. (4) because the disturbance frequency effect is neglected.

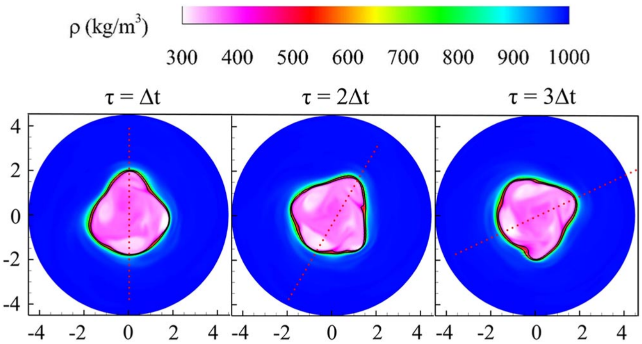

Fig. 12 Temporal evolution of density field at $x = 10$ mm ($x/R = 3.7$), $\Delta t = 0.06$ ms, and $p = 100$ atm.

Figure 12 shows the temporal evolution of the density field at $x = 10$ mm on the transverse plane. A trace of the wave crest in the flow transition region (denoted by the dotted line) in a single period shows that the characteristic frequency of the helical mode $m = -1$ is 1.6 kHz. The azimuthal wave speed in the transition region is estimated to be 27.4 m/s. The frequencies of all helical modes thus become

$$f_m = |m| \times 1.6\ \mathrm{kHz}, \quad m = \pm 1, \pm 2, \pm 3, \ldots \tag{5}$$

Thus, the frequency of the dominant helical mode $m = -3$ shown in Fig. 10 is 4.8 kHz.

D. Injector Flow Dynamics

The injector flow dynamics involve a wide range of time and length scales. Quantitative information can first be obtained using power spectral analysis. Figure 13 shows the selected probe positions in the LOX film data acquisition. They are well distributed in the vortex chamber and discharge nozzle, as well as immediately downstream of injector. Figure 14 shows the time histories of pressure fluctuations at probes 1, 8, 10, and 11 along the flow passage, where $t = 10$ ms refers to the start of the acquisition of statistically meaningful data. The pressure oscillates periodically at these locations, with low-frequency components dominant in the flowfield. High-frequency components become more prominent at probe locations 10 and 11, where the shear-layer instability is significant.

Figures 15 and 16 show the power spectral densities of pressure oscillations at various locations along the injector. The data were collected after the flow reached a statistically stationary state, over a time span of 8 ms. Flow instabilities were quantified and decomposed into various modes. High-frequency modes with small wavelengths were largely confined in the vortex chamber because of wave reflection between the head end and conical convergent section,

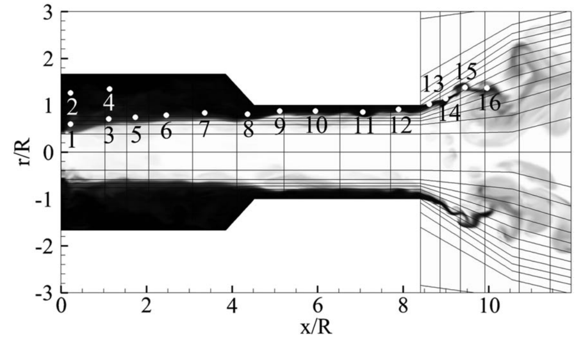

Fig. 13 Probe positions within the LOX.

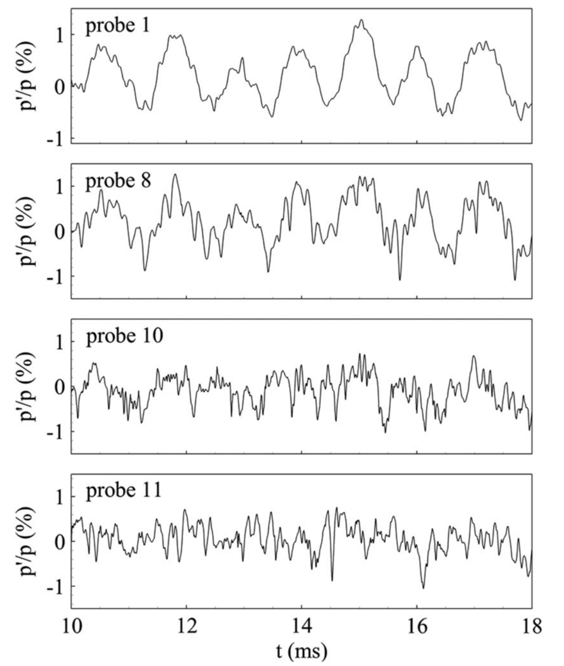

Fig. 14 Time histories of pressure fluctuations at four different probe locations.

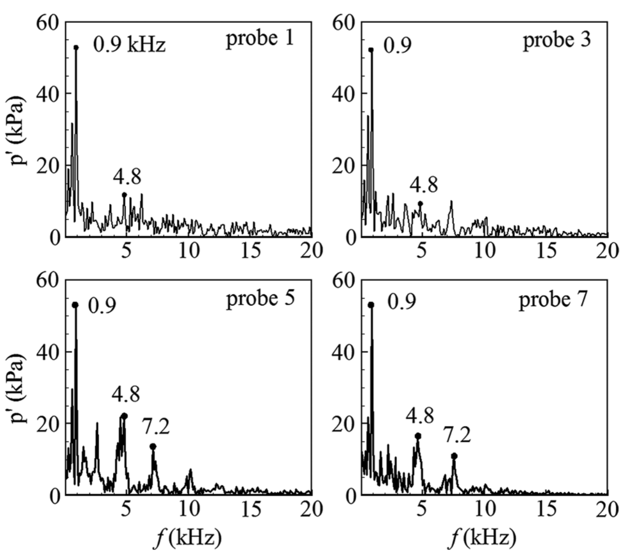

Fig. 15 Power spectral densities of pressure fluctuations at four different locations in the vortex chamber.

whereas low-frequency modes with long wavelengths could be transmitted to the discharge nozzle. Many of the flow disturbances thus remained in the vortex chamber, and the amplitude of wave motion decayed considerably as the waves traveled downstream. The dominant mode at a frequency of 0.9 kHz was observed within the injector. This frequency corresponded to the most amplified overall response of the injector with interactions of the tangential inlets, vortex chamber, and discharge nozzle.

Bazarov and Yang [14] suggested that the overall response function of a swirl injector $\prod_{\text{inj}}$ could be represented by the transfer characteristics of individual element of the injector:

$$\prod_{\text{inj}} = \left(\frac{R_v}{r_{\text{he}}}\right)^2 \frac{\prod_t \prod_{vn} \prod_n}{2\prod_t(\prod_{v2} + \prod_{v3}) + 1} \tag{6}$$

where $\prod_t$, $\prod_{vn}$, $\prod_{v2}$, $\prod_{v3}$, and $\prod_n$ are the transfer functions of the tangential inlets, nozzle entrance, vortex chamber due to surface waves, vortex chamber due to vorticity waves, and discharge nozzle, respectively. The averaged gaseous core radius at the head end is r_{he}. The explicit expressions of the elementary transfer functions were described by Bazarov et al. [3]. Ismailov and Heister [35] modified these transfer functions by improving the accuracy of wave speeds. Figure 17 shows the amplitude of the overall injector response as a function of the

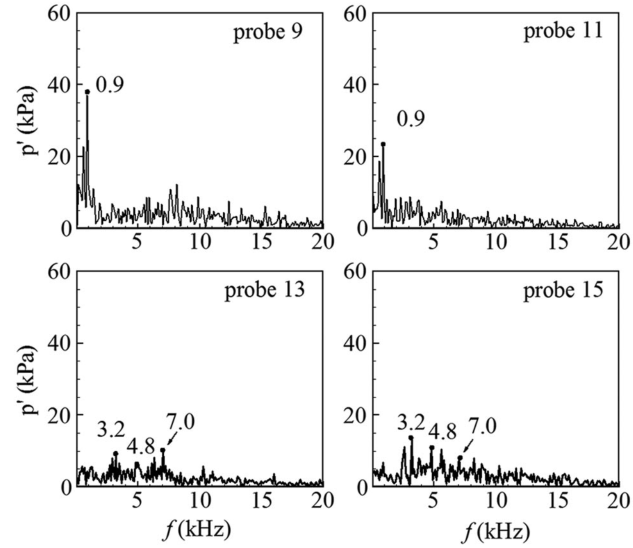

Fig. 16 Power spectral densities of pressure fluctuations at four different locations (probes 5–8) in the nozzle and near the injector exit.

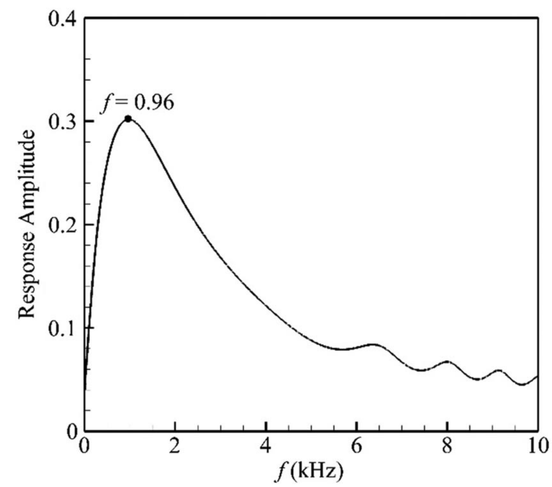

Fig. 17 Overall injector response as a function of disturbance frequency.

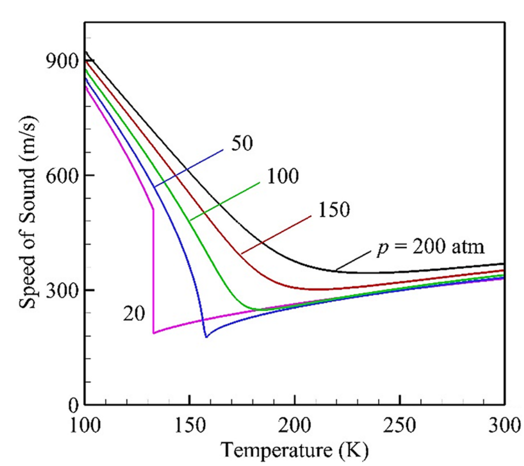

Fig. 18 Speed of sound of oxygen as a function of temperature at various pressures.

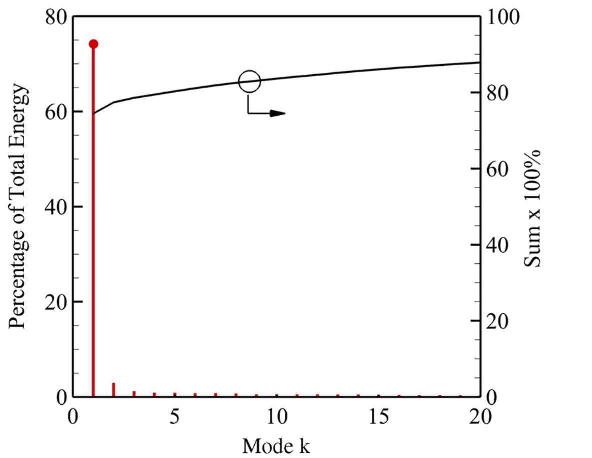

Fig. 19 Energy distribution of POD modes of pressure oscillation within the injector: $p = 100$ atm.

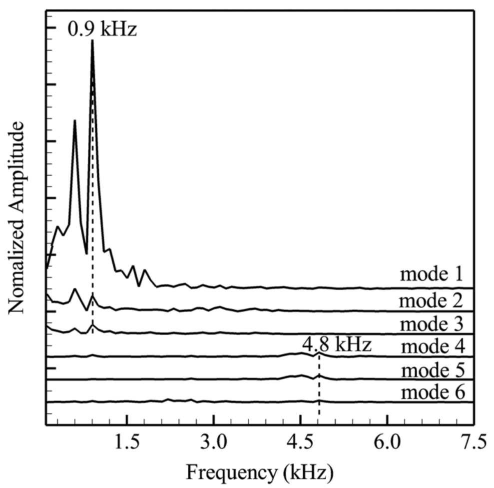

Fig. 20 Frequency spectra of time-varying coefficients of first six POD modes of pressure oscillations within the injector: $p = 100$ atm.

disturbance frequency, using Eq. (6). The frequency corresponding to the peak amplitude is 0.96 kHz, which is in good agreement with the dominant frequency of the simulation results. The difference from the 0.9 kHz dominant frequency seen in Figs. 15 and 16 may result from the assumption of inviscid and incompressible flows under Eq. (6).

The injector can be acoustically treated as a quarter-wave resonator, with a closed head end and an open exit. The fundamental frequency of the acoustic motion is determined by the following equation:

$$f = c/4(L + \Delta l) \tag{7}$$

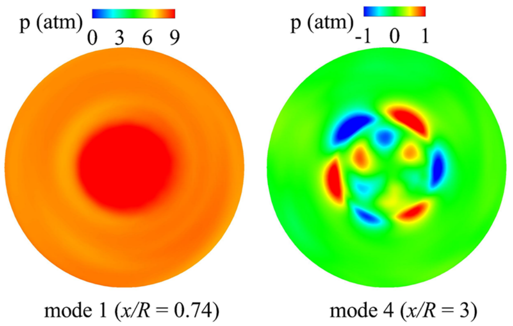

Fig. 22 Spatial distributions of mode 1 and mode 4 of the oscillatory pressure field on transverse (r–θ) plane within injector.

where L is the injector length; c is the speed of sound; and Δl is the correction factor, which is usually taken as $0.6R$. In the present study, the oxygen goes from subcritical to supercritical along the radial direction. The speed of sound changes accordingly. Figure 18 shows the speed of sound in oxygen as a function of temperature for given pressures. It first decreases, reaches a minimum at the phase transition, and then increases with increasing temperature. The average speed of sound within the whole injector, estimated as 470 m/s, is used to compute the acoustic frequency, which can be seen from Eq. (7) to be 4.8 kHz. The acoustic wave identifies and resonates with the helical mode $m = -3$ at the same frequency (4.8 kHz) in the vortex chamber. This explains the flow pattern of the three major structures seen in Fig. 10.

As the liquid oxygen exits the injector, flow instabilities develop due to the strong interactions of the outer shear layer and the center recirculation zone. When these waves reach a certain energy level, they roll up into vortices. The initial vortex shedding frequency f_i is determined by the characteristics of the exit velocity profile [36]:

$$f_i = St_i \bar{U}/\theta_0 \tag{8}$$

where the Strouhal number St_i ranges from 0.044 to 0.048 for turbulent flows, and the momentum thickness θ_0 is nearly 0.135 mm at the injector exit. The mean axial velocity $\bar{U}$ is around 20 m/s. The predicted initial vortex shedding frequency is 6.5 kHz, which is comparable to one of the peak values (7.0 kHz) in Fig. 16. As vortices move downstream, they interact and merge to oscillate at the subharmonics of the initial vortex shedding frequency. The cutoff frequency, also known as the preferred-mode frequency f_p [36], exists when the pairing process is terminated further downstream. Note that f_p is characterized by a preferred-mode Strouhal number ($St_p = 0.25$–0.5), nozzle radius R, and mean velocity $\bar{U}$. The calculated f_p ($= St_p \bar{U}/R$) is 3.7 kHz, which is comparable to 3.2 kHz in Fig. 16 and falls roughly in the second subharmonic mode of the initial frequency f_i.

The injector flow dynamics are further explored using the proper orthogonal decomposition technique to extract dynamically significant structures from the flowfield of concern [37]. For a

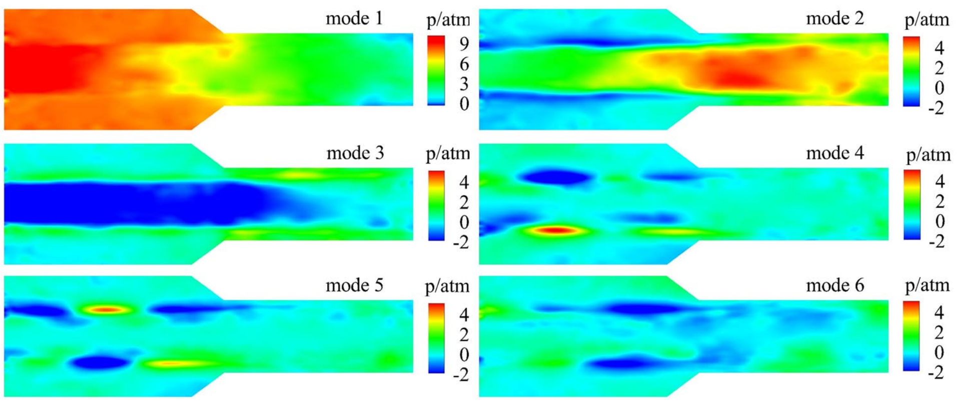

Fig. 21 Spatial distributions of the first six POD modes of the oscillatory pressure field on the longitudinal (x–r) plane within the injector: $p = 100$ atm.

Table 2 Effects of injector geometry and flow conditions on LOX film thickness and spreading angle at injector exit

Case	Geometry	p, atm	T, K	h_T, mm	h_ρ, mm	2α, deg
1	3-D	69	300	0.809	0.446	107.1
2	3-D	100	300	0.612	0.419	104.0
3	3-D	200	300	0.532	0.392	102.1
4	3-D	100	600	0.514	0.500	103.1
5	Axisymmetric	100	300	0.392	0.324	97.9

given flow property $[f(\boldsymbol{x}, t)]$, the POD analysis can determine a set of orthogonal functions $[\varphi_j(\boldsymbol{x}),\ j = 1, 2, \ldots]$, such that the projection of $f(\boldsymbol{x}, t)$ onto the first n base functions

$$\hat{f}(\boldsymbol{x}, t) = \bar{f}(\boldsymbol{x}) + \sum_{j=1}^{n} a_j(t)\varphi_j(\boldsymbol{x}) \tag{9}$$

has the smallest error, defined as $E(\|f - \hat{f}\|)$. Here, $\boldsymbol{x}$ is the spatial coordinate in the three-dimensional space and $a_j(t)$ represents the temporal variation of the jth mode. $E(\cdot)$ and $\|\cdot\|$ denote the time average and L^2-norm in the space, respectively. The scalar function f can be extended to a vector $\boldsymbol{F}$ by introducing an appropriate inner product. A more complete discussion of this subject can be found in [38]; the present work focuses primarily on the oscillating pressure field. The POD analysis was conducted for the entire three-dimensional (3-D) flowfield within the injector. A total of 333 snapshots were acquired with a time interval of 30 μs between two consecutive snapshots (compare to the time step of 1 μs in the numerical simulation). The frequency resolution covers a range of 0.1–33 kHz.

Figure 19 shows the energy distribution of the POD modes according to the oscillatory pressure field. Mode 1 occupies 74% of the total energy, and the first six modes take more than 80% of the total energy of the oscillatory field. Figure 20 shows the frequency spectra of the time-varying coefficients $a_j(t)$ of these modes. The first three modes have the same peak frequency of 0.9 kHz and are closely related to hydrodynamic instability waves representing the most significant injector responses, whereas the other three modes share the dominant frequency of 4.8 kHz, which represents acoustic motion.

Figure 21 shows the spatial distribution of the first six POD modes of the oscillatory pressure field on a longitudinal plane. The first mode exhibits a descending trend along the axial direction with a maximum at the head end. The second and third modes show a pattern similar to that of the first mode, but with much weaker strength and different phase angles. The fourth, fifth, and sixth modes also have a similar shape, but with different phase angles, and are closely related to the acoustic and helical waves, as discussed previously, with the characteristic frequency of 4.8 kHz. Figure 22 shows the spatial distributions of modes 1 and 4 on the transverse plane. The nearly uniform pressure distribution of mode 1 implies that the disturbance propagates mainly in the longitudinal direction. The well-organized structure of mode 4 with three distinctive wave lengths further confirms the existence of the helical mode of $m = -3$.

E. Effects of Flow Conditions

The effects of pressure and temperature on the injector dynamics are studied. Table 2 lists the five cases of concern. Cases 1–4 are at different conditions, with the same three-dimensional geometry. Case 5 has the same operating conditions as case 2, but with an axisymmetric configuration. Figure 23 shows the distributions of the azimuthally averaged mean density for cases 1–4. The density in the gaseous core increases with pressure, whereas it decreases significantly as the temperature varies from 300 to 600 K. At $p = 200$ atm, the minimum density of oxygen in the chamber exceeds 260 kg/m^3. Figure 24 shows the corresponding density gradient fields. The transition of the fluid state near the LOX film surface is clearly observed. The radius of the gaseous core decreases with increasing pressure. The region of steep density gradient extends to a broader area downstream of the injector as the pressure increases. As the chamber temperature changes from 300 (cases 1–3) to 600 K (case 4), the density variation decreases considerably, but the central gaseous core grows significantly.

Under supercritical conditions, the distinct interface between the liquid and gas phases commonly observed at subcritical pressure is replaced by a continuous transition region. The liquid film thickness thus cannot be clearly defined. Huo et al. [20] introduced two different ways to identify the film thickness for a given axial location. One was based on the distance between the surface of maximum density gradient and the injector wall along the radial direction h_ρ. The other was the distance between the surface of the critical temperature and the injector wall h_T. Table 2 lists the LOX film thickness at the injector exit using both definitions. The film thickness based on the critical temperature is higher than that based on the maximum density gradient, although the trend of its variation with pressure is similar. The film thickness increases slightly with increasing pressure for the 3-D cases. Figure 25 extracts the location of the maximum density gradient in the radial direction as a function of axial coordinate. The difference in film thickness at various pressures is relatively small for the 3-D cases. The LOX film in the axisymmetric case (case 5) is thinner than that in the 3-D case (case 2). The viscous loss through the swirling passage in the injector is lower in case 5, leading to higher axial and radial momentum fluxes.

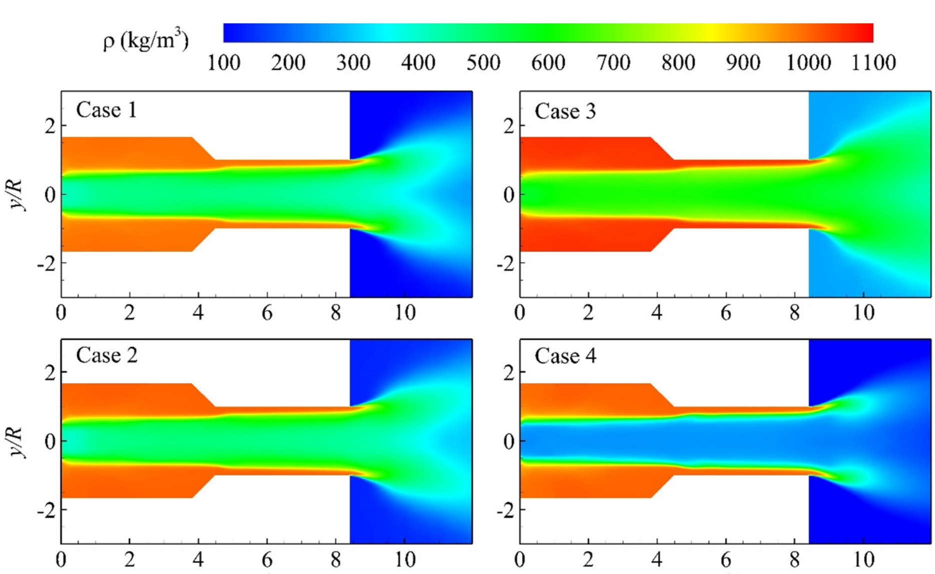

Fig. 23 Distributions of azimuthally averaged density field for cases 1–4.

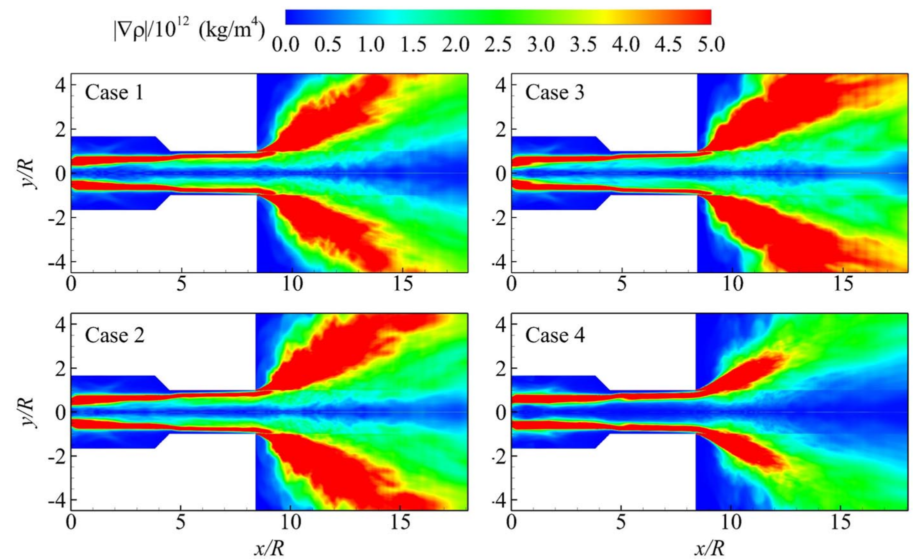

Fig. 24 Distributions of the magnitude of azimuthally averaged density gradient for cases 1–4.

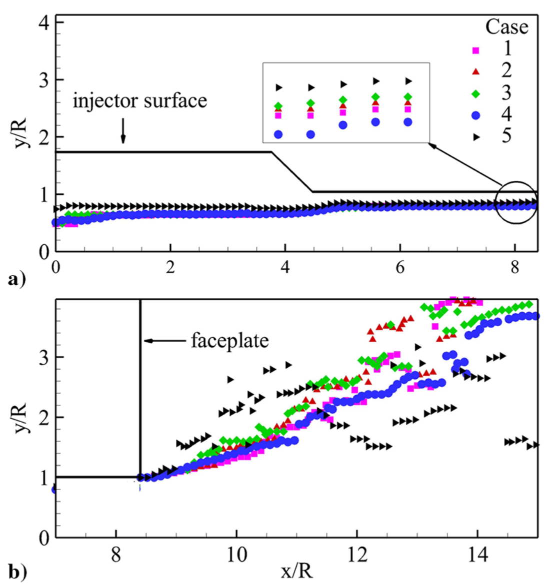

Fig. 25 Distributions of local maximum density gradient in the radial direction as a function of the axial coordinate a) within the injector, and b) downstream of the injector.

The liquid film thickness is therefore thinner because of the conservation of mass.

Figure 25b also provides information on LOX film spreading, which is an indication of liquid atomization and mixing. Here, the spreading angle is defined as twice the angle between the dotted symbols and the axial centerline in the chamber. The chamber pressure has negligible influence, although the spreading angle decreases slightly with increasing temperature. It is noteworthy that the axisymmetric study (case 5) yields a much higher spreading angle than the 3-D studies (cases 1–4). Table 2 lists the spreading angle calculated from velocity components at the injector exit: $\alpha = \tan(u_\theta/u_x)$. The computed angles for the 3-D studies are larger than that for the axisymmetric study. This discrepancy suggests that the angle obtained from velocity components may not properly represent film spreading. Instead, the angles visualized from the curves of maximum density gradient exhibit the physical behavior of spreading and are useful for exploring the influences of various parameters.

VI. Conclusions

A comprehensive investigation of LOX swirl injector flow dynamics has been performed at supercritical conditions. A unified theoretical and numerical framework for general fluids was implemented, along with the large-eddy simulation technique. The complex 3-D flow structures were presented for the first time. Unlike the interface between liquid and gas at subcritical pressure, a smooth fluid transition region was identified at supercritical pressure. Various flow instability mechanisms, including shear-layer instability, acoustic instability, centrifugal instability, and helical instability, were evaluated using the spectral analysis and proper orthogonal decomposition techniques. Hydrodynamic instability was found to play a dominant role in flow oscillations across the injector, and the corresponding characteristic frequency determined by numerical simulations showed good agreement with the prediction of the analytical response transfer function of a swirl injector. The helical mode $m = -3$ resonated with the acoustic wave at 4.8 kHz and amplified itself significantly as compared to other modes. The converging section reflected the waves back into the vortex chamber and only allowed some of waves with long wavelengths to be transmitted to the discharge nozzle.

A parametric study was also conducted to examine the influence of flow conditions and geometry on the injector characteristics. The gaseous core decreased with increasing pressure. The liquid film thickness increased slightly with pressure. An axisymmetric study produced a smaller film thickness and larger spreading angle than 3-D studies due to the lack of flow dynamics in the azimuthal direction and lower momentum loss. The spreading angle defined by the maximum density gradient provided a more physical interpretation of liquid spreading than the conventional definition of the ratio of axial and tangential velocity components. The spreading angle was nearly independent of the pressure. The results reported here provide a basis for future research on the mixing and combustion of swirling flows at supercritical conditions.

Acknowledgments

This work was sponsored by the U.S. Air Force Office of Scientific Research under grant no. FA 9550-10-1-0179. The authors gratefully acknowledge support and advice given by Mitat A. Birkan.

References

[1] Lieuwen, T. C., and Yang, V., (eds.), *Combustion Instabilities in Gas Turbine Engines (Operational Experience, Fundamental Mechanisms and Modeling)*, Vol. 210, Progress in Astronautics and Aeronautics, AIAA, Reston, VA, 2005.
doi:10.2514/4.866807

[2] Huang, Y., and Yang, V., "Dynamics and Stability of Lean-Premixed Swirl-Stabilized Combustion," *Progress in Energy and Combustion Science*, Vol. 35, No. 4, 2009, pp. 293–364.
doi:10.1016/j.pecs.2009.01.002

[3] Bazarov, V., Yang, V., and Puri, P., "Design and Dynamics of Jet and Swirl Injectors," *Liquid Rocket Thrust Chambers: Aspects of Modeling, Analysis, and Design*, Vol. 200, Progress in Astronautics and Aeronautics, edited by V. Yang, M. Habiballah, J. Hulka, and M. Popp, AIAA, Reston, VA, 2004, pp. 19–103. doi:10.2514/4.866760

[4] Rizk, N., and Lefebvre, A., "Internal Flow Characteristics of Simplex Swirl Atomizers," *Journal of Propulsion and Power*, Vol. 1, No. 3, 1985, pp. 193–199. doi:10.2514/3.22780

[5] Inamura, T., Tamura, H., and Sakamoto, H., "Characteristics of Liquid Film and Spray Injected from Swirl Coaxial Injector," *Journal of Propulsion and Power*, Vol. 19, No. 4, 2003, pp. 632–639. doi:10.2514/2.6151

[6] Fu, Q.-F., Yang, L.-J., Zhang, W., and Cui, K.-D., "Spray Characteristics of an Open-End Swirl Injector," *Atomization and Sprays*, Vol. 22, No. 5, 2012, pp. 431–445. doi:10.1615/AtomizSpr.v22.i5

[7] Ahn, K., Han, Y.-M., and Choi, H.-S., "Effects of Recess Length on Discharge Coefficients of Swirl Coaxial Injectors," *Combustion Science and Technology*, Vol. 184, No. 3, 2012, pp. 323–336. doi:10.1080/00102202.2011.635615

[8] Fu, Q., and Yang, L., "Visualization Studies of the Spray from Swirl Injectors Under Elevated Ambient Pressure," *Aerospace Science and Technology*, Vol. 47, Dec. 2015, pp. 154–163. doi:10.1016/j.ast.2015.09.027

[9] Kim, D., Im, J.-H., Koh, H., and Yoon, Y., "Effect of Ambient Gas Density on Spray Characteristics of Swirling Liquid Sheets," *Journal of Propulsion and Power*, Vol. 23, No. 3, 2007, pp. 603–611. doi:10.2514/1.20161

[10] Kenny, R. J., Hulka, J. R., Moser, M. D., and Rhys, N. O., "Effect of Chamber Backpressure on Swirl Injector Fluid Mechanics," *Journal of Propulsion and Power*, Vol. 25, No. 4, 2009, pp. 902–913. doi:10.2514/1.38537

[11] Chen, X., and Yang, V., "Effect of Ambient Pressure on Liquid Swirl Injector Flow Dynamics," *Physics of Fluids*, Vol. 26, No. 10, 2014, Paper 102104. doi:10.1063/1.4899261

[12] Cho, S., Park, G., Chung, Y., Yoon, Y., and Bazarov, V. G., "Surface Instability on Cryogenic Swirl Flow at Sub-to Supercritical Conditions," *Journal of Propulsion and Power*, Vol. 30, No. 4, 2014, pp. 1038–1046. doi:10.2514/1.B35071

[13] Cho, S., Kim, H., Yoon, Y., and Sung, H.-G., "Dynamic Characteristics of a Cryogenic Swirl Flow Under Supercritical Conditions," *Aerospace Science and Technology*, Vol. 51, No. 4, 2016, pp. 162–170. doi:10.1016/j.ast.2016.02.008

[14] Bazarov, V. G., and Yang, V., "Liquid-Propellant Rocket Engine Injector Dynamics," *Journal of Propulsion and Power*, Vol. 14, No. 5, 1998, pp. 797–806. doi:10.2514/2.5343

[15] Wang, S., and Yang, V., "Unsteady Flow Evolution in Swirl Injectors with Radial Entry. II. External Excitations," *Physics of Fluids (1994-Present)*, Vol. 17, No. 4, 2005, Paper 045107. doi:10.1063/1.1874932

[16] Ismailov, M., and Heister, S. D., "Dynamic Response of Rocket Swirl Injectors, Part I: Wave Reflection and Resonance," *Journal of Propulsion and Power*, Vol. 27, No. 2, 2011, pp. 402–411. doi:10.2514/1.B34044

[17] Ismailov, M., and Heister, S. D., "Dynamic Response of Rocket Swirl Injectors, Part II: Nonlinear Dynamic Response," *Journal of Propulsion and Power*, Vol. 27, No. 2, 2011, pp. 412–421. doi:10.2514/1.B34045

[18] Yang, V., "Modeling of Supercritical Vaporization, Mixing, and Combustion Processes in Liquid-Fueled Propulsion Systems," *Proceedings of the Combustion Institute*, Vol. 28, No. 1, 2000, pp. 925–942. doi:10.1016/S0082-0784(00)80299-4

[19] Zong, N., and Yang, V., "Cryogenic Fluid Dynamics of Pressure Swirl Injectors at Supercritical Conditions," *Physics of Fluids*, Vol. 20, No. 5, 2008, Paper 056103. doi:10.1063/1.2905287

[20] Huo, H., Zong, N., and Yang, V., "Cryogenic Fluid Dynamic Response of Swirl Injector to External Forcing at Supercritical Conditions," AIAA Paper 2009-0233, 2009. doi:10.2514/6.2009-233

[21] Wang, X., Huo, H., Wang, Y., Zhang, L., and Yang, V., "A Three-Dimensional Analysis of Swirl Injector Flow Dynamics at Supercritical Conditions," AIAA Paper 2015-1827, 2015. doi:10.2514/6.2015-1827

[22] Oefelein, J. C., and Yang, V., "Modeling High-Pressure Mixing and Combustion Processes in Liquid Rocket Engines," *Journal of Propulsion and Power*, Vol. 14, No. 5, 1998, pp. 843–857. doi:10.2514/2.5349

[23] Erlebacher, G., Hussaini, M., Speziale, C., and Zang, T., "Toward the Large-Eddy Simulation of Compressible Turbulent Flows," *Journal of Fluid Mechanics*, Vol. 238, May 1992, pp. 155–185. doi:10.1017/S0022112092001678

[24] Wang, X., Huo, H., and Yang, V., "Supercritical Combustion of General Fluids in Laminar Counterflows," AIAA Paper 2013-1165, 2013. doi:10.2514/6.2013-1165

[25] Huo, H., Wang, X., and Yang, V., "A General Study of Counterflow Diffusion Flames at Subcritical and Supercritical Conditions: Oxygen/Hydrogen Mixtures," *Combustion and Flame*, Vol. 161, No. 12, 2014, pp. 3040–3050. doi:10.1016/j.combustflame.2014.06.005

[26] Wang, X., Huo, H., and Yang, V., "Counterflow Diffusion Flames of Oxygen and N-Alkane Hydrocarbons (CH4-C16H34) at Subcritical and Supercritical Conditions," *Combustion Science and Technology* Vol. 187, Nos. 1–2, 2014, pp. 60–82. doi:10.1080/00102202.2014.973955

[27] Meng, H., and Yang, V., "A Unified Treatment of General Fluid Thermodynamics and Its Application to a Preconditioning Scheme," *Journal of Computational Physics*, Vol. 189, No. 1, 2003, pp. 277–304. doi:10.1016/S0021-9991(03)00211-0

[28] Zong, N., and Yang, V., "An Efficient Preconditioning Scheme for Real-Fluid Mixtures Using Primitive Pressure-Temperature Variables," *International Journal of Computational Fluid Dynamics*, Vol. 21, Nos. 5–6, 2007, pp. 217–230. doi:10.1080/10618560701584373

[29] Hsieh, S.-Y., and Yang, V., "A Preconditioned Flux-Differencing Scheme for Chemically Reacting Flows at All Mach Numbers," *International Journal of Computational Fluid Dynamics*, Vol. 8, No. 1, 1997, pp. 31–49. doi:10.1080/10618569708940794

[30] Swanson, R. C., and Turkel, E., "On Central-Difference and Upwind Schemes," *Journal of Computational Physics*, Vol. 101, No. 2, 1992, pp. 292–306. doi:10.1016/0021-9991(92)90007-L

[31] Rubinsky, V. R., "Instability Phenomenology and Case Studies: Combustion Instability in the RD-0110 Engine," *Liquid Rocket Engine Combustion Instability*, Vol. 169, Progress in Astronautics, and Aeronautics, edited by V. Yang, and W. E. Anderson, AIAA, Reston, VA, 1995, pp. 89–112. doi:10.2514/5.9781600866371.0089.0112

[32] Li, H.-G., Zong, N., Lu, X.-Y., and Yang, V., "A Consistent Characteristic Boundary Condition for General Fluid Mixture and Its Implementation in a Preconditioning Scheme," *Advances in Applied Mathematics and Mechanics*, Vol. 4, No. 1, 2012, pp. 72–92. doi:10.4208/aamm.11-m1160

[33] Wang, X., and Yang, V., "Supercritical Mixing and Combustion of Liquid-Oxygen/Kerosene Bi-Swirl Injectors," *Journal of Propulsion and Power*, Vol. 33, No. 2017, pp. 316–322. doi:10.2514/1.B36262

[34] Wang, X., Wang, Y., and Yang, V., "Geometric Effects on Liquid Oxygen/Kerosene Bi-Swirl Injector Flow Dynamics at Supercritical Conditions," *AIAA Journal*, 2017. doi:10.2514/1.J055952

[35] Ismailov, M., and Heister, S., "Nonlinear Modeling of Classical Swirl Injector Dynamics," AIAA Paper 2009-5402, 2009. doi:10.2514/6.2009-5402

[36] Schadow, K., and Gutmark, E., "Combustion Instability Related to Vortex Shedding in Dump Combustors and Their Passive Control," *Progress in Energy and Combustion Science*, Vol. 18, No. 2, 1992, pp. 117–132. doi:10.1016/0360-1285(92)90020-2

[37] Huang, Y., Wang, S., and Yang, V., "Systematic Analysis of Lean-Premixed Swirl-Stabilized Combustion," *AIAA Journal*, Vol. 44, No. 4, 2006, pp. 724–740. doi:10.2514/1.15382

[38] Berkooz, G., Holmes, P., and Lumley, J. L., "The Proper Orthogonal Decomposition in the Analysis of Turbulent Flows," *Annual Review of Fluid Mechanics*, Vol. 25, No. 1, 1993, pp. 539–575. doi:10.1146/annurev.fl.25.010193.002543

J. P. Drummond
Associate Editor